https://doi.org/10.2352/ISSN.2470-1173.2020.14.COIMG-305
© 2020, Society for Imaging Science and Technology

Connected-Tube MPP Model for Unsupervised 3D Fiber Detection

Tianyu Li[1], Camilo G. Aguilar[1], Ronald F. Agyei[2], Imad A. Hanhan[2], Michael D. Sangid[2], Mary L. Comer[1];
[1]School of Electrical and Computer Engineering, [2]School of Aeronautics and Astronautics; Purdue University, West Lafayette, IN

Abstract

In this paper, we extend our previous 2D connected-tube marked point process (MPP) model to a 3D connected-tube MPP model for fiber detection. In the 3D case, a tube is represented by a cylinder model with two spherical areas at its ends. The spherical area is used to define connection priors that encourage connection of tubes that belong to the same fiber. Since each long fiber can be fitted by a series of connected short tubes, the proposed model is capable of detecting curved long tubes. We present experimental results on fiber-reinforced composite material images to show the performance of our method.

1. INTRODUCTION

Due to their excellent strength-to-weight ratio, short fiber reinforced composites (SFRC) are potential candidate materials in numerous aerospace and automobile light-weight applications. Injection molding, the main manufacturing process associated with SFRCs, enables large-scale production of simple to highly geometrically complex parts, which have considerable variation of the microstructure. It is known that a material's physical properties are crucially linked to its microstructure [1-4]. Thus, to connect material response with the underlying heterogeneity, robust characterization methods and models are required to provide a promising platform of quantitatively describing the structural features [5-6]. In this work, we focus on the task of fiber detection in X-ray tomography images. Most popular deep learning methods, such as the U-Net [7], cannot be directly applied to this task due to the lack of labeled data. So only unsupervised detection methods will be discussed here.

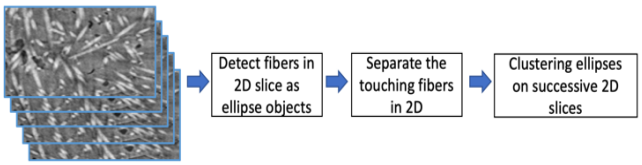

***Figure 1**. Previous pipeline of fiber detection from 2D to 3D.*

With the assumption that a 2D slice of a cylindrical fiber can be characterized by an ellipse, with the major and minor axe of the ellipse indicating the orientation of the fiber, localizing fibers in 3D space has previously been realized by the pipeline shown in Figure 1. First, fibers in 2D tomography slices are extracted as ellipse objects by a 2D ellipse fitting method. Then extracted ellipse objects are converted into binary images and a watershed segmentation algorithm is applied to the binary images for separating the touching fibers. Finally, matching ellipses on successive 2D slices are stacked to localize the fibers in 3D. There are mainly two drawbacks of the above method. First, the fibers in 2D slices may not be characterized by ellipses well. This can be seen in Figure 2. In this example, an ellipse marked point process model is applied to a 2D microscopy slice. The long fibers cannot be detected as its shape does not fit well with the ellipse; also the fibers in the green rectangles are missed due to close contact of fibers.

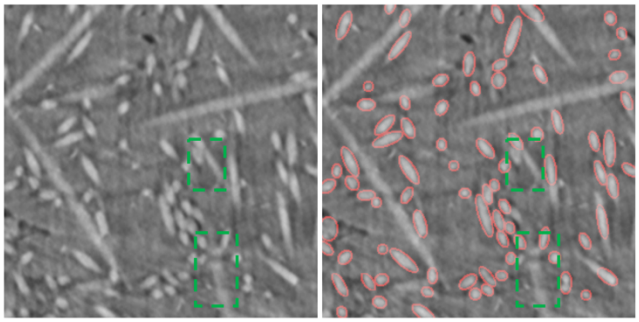

***Figure 2**. An example of fiber detection in 2D slice.*

Moreover, in the step of clustering ellipses on successive 2D slices, errors such as clustering two different fibers into one could happen when two fibers closely contact each other.

Considering the problems in 2D-3D fiber detection methods, modeling and detecting fibers in 3D directly could be a better solution, since the fiber can be better modeled in 3D and the step of clustering ellipses is no longer needed.

Marked point process (MPP) modeling [8] provides a framework for the task of detecting fibers in 3D directly. As a stochastic approach for object detection, it is useful for modeling the random locations of objects in images. It has already achieved success in many object detection applications [9, 10].

Intuitively, a fiber could be associated with a cylinder in the MPP framework. However, there are two problems with a cylinder shape model. One is that the length of a fiber can vary over a wide range, which will result in a huge computational burden in the sampling process. The other is that not all fibers are straight. The cylinder model cannot model curved fibers well.

In order to model the fibers properly, we extend our previous 2D connected-tube MPP model [11] into a 3D version. In the 3D connected-tube MPP model, each fiber is modeled as a series of connected short tubes rather than a single cylinder. To accelerate the detection process, we introduce a grow kernel in optimization which allows more birth of new tubes near the ends of current tubes.

This paper is organized as follows: In Section 2, we describe the 3D connected-tube MPP model. In Section 3, the optimization method is discussed. In Section 4, experimental results for synthetic fiber images and real fiber-reinforced composite materials images are presented. Conclusions are given in Section 5.

2. 3D Connected-tube MPP model

Let Y be the observed 3D image and $S = [0, X_{max}] \times [0, Y_{max}] \times [0, Z_{max}]$ the image lattice, $S \subset R^3$. A point process on S is a set of points $\{S_1, S_2, \dots, S_n\} \subseteq S$, with random variable S_i representing the random location of the ith point. In a marked point process, for each S_i, there is an associated mark, which consists of random variables from a mark space M describing an object located at point i. For our 3D connected-tube MPP model, the mark of a tube represents a cylinder, which is defined by the vector $(r, h, \theta^Y, \theta^Z)$, as in Figure 3. The random variable r is the minor semi-axis length (radius), h is the major semi-axis length (semi-height). $\theta^Y \in [0, \pi]$ and $\theta^Z \in [0, \pi]$ control the orientation of the tube. To determine the orientation of a tube, consider an erect tube which is vertical to the $x - y$ plane, first rotated around the y axis in the clockwise direction by θ^Y, then rotated around the z axis in the counter-clockwise direction by θ^Z. The mark space is given as $M = [r_{min}, r_{max}] \times [h_{min}, h_{max}] \times [0, \pi] \times [0, \pi]$, for some parameters r_{min}, r_{max}, h_{min}, h_{max}. A marked object is defined as a vector $W_i = (S_i, M_i) \in W$, where $W \subseteq S \times M$. Let Ω_w be the configuration space, which denotes the space of all possible realizations of W. Then $w = (w_1, w_2, \dots, w_n) \in \Omega_w$ is a possible object configuration, where n is the number of objects in this configuration.

The Gibbs density of the marked point process is given by

$$f(w|y) = \frac{1}{Z} exp\{-V_d(y|w) - V_p(w)\} \quad (1)$$

where y denotes the observed 3D image, Z is the normalizing constant (also called the partition function), $V_d(y|w)$ is the data energy, which describes how well the objects fit the observed image data y. $V_p(w)$ is the prior energy introducing the prior knowledge on the object configuration.

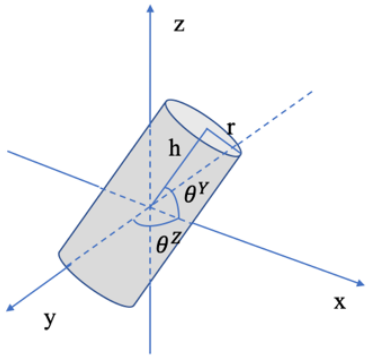

***Figure 3**. The 3D tube model.*

2.1. Data Energy

Data energy $V_d(y|w)$ is modeled as the sum of the individual object energies:

$$V_d(y|w) = \sum_i V_d(y|w_i) \quad (2)$$

where $V_d(y|w_i)$ describes how well object w_i fits the observed image y. We define an inner region D^{in} and outer region D^{out} for each object, as shown in Figure 4. D^{in} is the set of pixels in the inner cylinder, and D^{out} is the set of pixels in the outer cylinder but not in the inner cylinder. By defining the Bhattacharya distance $B(y|w_i)$ between D^{in} and D^{out} of each object w_i, $V_d(y|w_i)$ can be calculated as in [10]:

$$V_d(y|w_i) = \begin{cases} 1 - \frac{B(y|w_i)}{T} & B(y|w_i) < T \\ exp\left(-\frac{B(y|w_i) - T}{3B(y|w_i)} - 1\right) & else \end{cases} \quad (3)$$

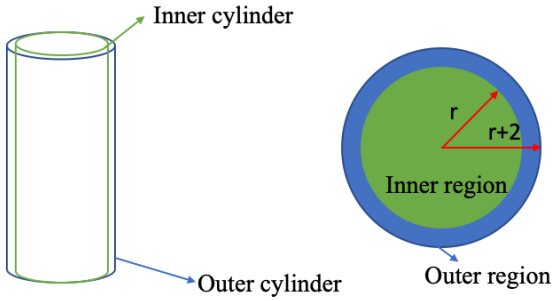

***Figure 4**. The inner region and outer region of a tube.*

2.2. Prior Energy

$V_p(w)$ describes the prior knowledge about objects. It is similar to the prior energy in the 2D connected-tube MPP model [11]:

$$V_p = \alpha V_p^{ol}(w) + \beta V_p^{len}(w) + \lambda V_p^{con}(w) \quad (4)$$

where $V_p^{ol}(w)$ penalizes overlapping between objects; $V_p^{len}(w)$ penalizes the tubes with short semi-height; $V_p^{con}(w)$ encourages connections between tubes; α, β, λ are the weights for each term.

2.2.1 Overlap prior

The overlap prior $V_p^{ol}(w)$ is given as:

$$V_p^{ol}(w) = \sum_{i,j} V^{ol}(w_i, w_j) \quad (5)$$

$$V^{ol}(w_i, w_j) = \begin{cases} R(w_i, w_j) & if\ R(w_i, w_j) < T_{ol} \\ \infty & else \end{cases} \quad (6)$$

where T_{ol} is an overlap threshold; $R(w_i, w_j)$ is the mutual overlap ratio between object w_i and w_j defined as:

$$R(w_i, w_j) = \frac{\#(D_{w_i}^{in} \cap D_{w_i}^{out})}{\min(\#D_{w_i}^{in}, \#D_{w_i}^{out})} \quad (7)$$

where $\#A$ means number of pixels in set A.

2.2.2. Length prior

A shorter tube may not fit the observed image data Y properly as its orientation is sensitive to noise. Moreover, shorter tubes could greatly increase the dimension of an object configuration w. Thus $V_p^{len}(w)$ is introduced to penalize shorter tubes.

Let

$$V_p^{len}(w) = \sum_i V^{len}(y|w_i) \quad (8)$$

where $V^{len}(y|w_i) = \exp\big((h_{max} - h_i)/h_{max}\big)$, and h_i is the semi-height of tube w_i.

2.2.3. Connection prior

The connection prior $V_p^{con}(w)$ is used to encourage tubes to be connected.

$$V_p^{con}(w) = \sum_i V^{con}(w_i) \tag{9}$$

To calculate $V^{con}(w_i)$, we define the front and back joint region at the two ends of a tube. Unlike the joint region in 2D connected-tube MPP model [11], the joint regions are not defined by circles but balls, as on the left of Figure 5, where the blue ball is the front joint region and the red ball is the back joint region. We expect the joint regions of a tube to be overlapped with the joint regions of other tubes as in right of Figure 5. Then $V^{con}(w_i)$ is defined as:

$$V^{con}(w_i) = 0.5\times F^{con}(w_i) + 0.5\times B^{con}(w_i) \tag{10}$$

where $F^{con}(w_i) = 0.5 - R_f(w_i)$; $B^{con}(w_i) = 0.5 - R_b(w_i)$; $R_f(w_i)$ and $R_b(w_i)$ are the overlap ratio of object w_i's front and back joint regions respectively.

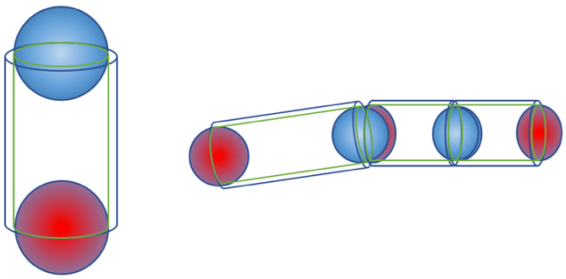

***Figure 5**. The front and back joint regions (left) and an example of connected tubes (right).*

3. Optimization

The optimization goal is to find an object configuration that maximizes the energy function $V_d(y|w) + V_p(w)$. We use the multiple birth and death algorithm proposed by Descombes et al. [12] to realize this goal. There are three types of kernel used for the state transitions in the configuration space: birth and death kernel, grow kernel and local perturbation kernel.

Birth and death kernel allows an object to be added or removed from the current object configuration w. In the framework of the multiple birth and death algorithm, each voxel that is not associated with current objects in the image lattice S has the same probability to give a birth of a new object.

Grow kernel is used to give birth of objects close to the joint regions of current objects in w. For an object w_i, if its front/back joint region is not overlapping with the joint region of other objects, then a new object w_{new} will be added close to its front/back joint region with grow rate g_rate, which is updated by $g\_rate = \sigma g\_rate$ in each iteration of the multiple birth and death algorithm with decay factor σ. As in Figure 6, if we grow from the right side of object w_i, one end of the new object w_{new} will be fixed at point A, which is the center of w_i's right end. For the other end of w_{new}, we assume it is uniformly distributed in the blue ball, which is centered around point B with radius h_i. B is extended from A along the major semi-axis of w_i with distance $2h_i$. One possible new object is the w_{new} with end points A and C in Figure 6.

Local perturbation kernel changes the marks h_i, r_i, θ_i^Y, θ_i^Z for each object w_i in w. Gaussian distributions are chosen to update these marks.

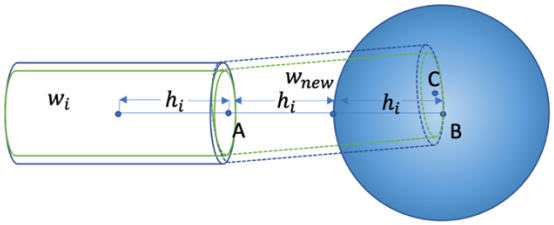

***Figure 6**. Illustration of the grow kernel.*

4. Experiments

Because of a lack of labeled ground truth of our fiber-reinforced composite materials images, we test our method on synthetic fiber images first. Then qualitative results of fiber detection in the real fiber images are presented.

In the experiments, the parameters of our model are set as $T = 50$, $T_{ol} = 0.25$, $r_{min} = 2$, $r_{max} = 5$, $h_{min} = 2$, $h_{max} = 8$, $\alpha = 0.5, \beta = 0.12$, $\lambda = 0.38$, g_rate is initialized with 1, $\sigma = 0.98$. All the parameters are set by trial and error. The algorithm is realized by C++ with OpenCV 2.4.9. The CPU in our experiments is Intel(R) Xeon(R) CPU E5-2690 2.90GHz.

4.1. Synthetic data

We generate 4 groups of image series by setting non-overlapped cylinders in 3D space with white noise. In each group, there are 128 2D slices with size 128×128. The first row of Figure 7 shows an example of 4 successive synthetic 2D slices. The second row presents the corresponding detection results. The third row is the ground truth. The bottom row is our binarized detection results. The 3D visualization of our detection results in this example is given in Figure 8. The precision and recall are used for measuring the results:

$$Precision = \frac{TP}{TP+FP} \tag{11}$$

$$Recall = \frac{TP}{TP+FN} \tag{12}$$

where TP is true positive, FP is false positive, FN is false negative. The quantitative results are shown in Table 1. We point out that the relatively low precision and recall are caused mostly by incorrect classification of voxels on the surface of fibers. To see this, we also count TP, FP and FN in a different way: if a voxel segmented as fiber is within $\sqrt{2}$ voxel's distance of a voxel in ground truth then this voxel is TP; if a voxel segmented as fiber is not within $\sqrt{2}$ voxel's distance of a voxel in ground truth then this voxel is FP; if a voxel in ground truth is not within $\sqrt{2}$ voxel's distance of a voxel in segmentation then this voxel is FN. The tolerance of $\sqrt{2}$ voxel in distance is used to ignore the false segmentation on the surface of fibers. The alternate test results are given in Table 2. These results imply that the proposed algorithm can localize most fibers correctly. Note that in real microcopy or

X-ray tomography datasets, there is often uncertainty in classifying voxels at object boundaries, due to limited spatial resolution, so it is often not possible to determine the correct classification of boundary voxels in practice either. The average running time for each group of data is 45 second.

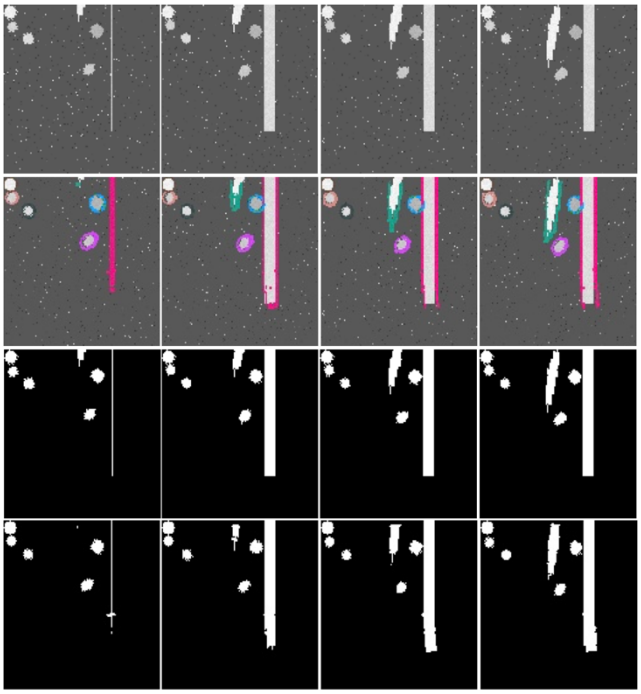

Figure 7. *One example of fiber detection in synthetic data (first row: original image slices; second row: detection results; third row ground truth of segmentation; fourth row: binarized fiber detection results).*

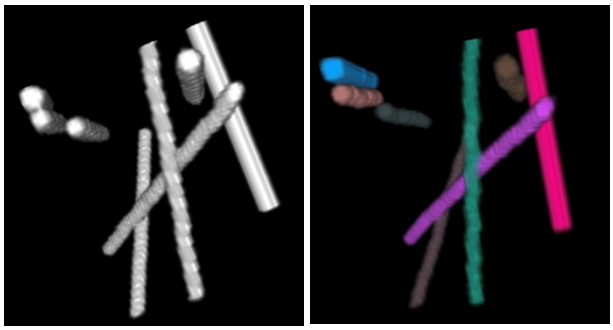

Figure 8. *3D visualization of fiber ground truth (left) and fiber detection results(right).*

Table 1: The quantitative test results on synthetic data.

	SynData1	SynData2	SynData3	SynData4
Prec	0.849	0.865	0.879	0.846
Recall	0.820	0.690	0.850	0.782

Table 2: The non-strict test results on synthetic data.

	SynData1	SynData2	SynData3	SynData4
Prec	0.995	0.998	0.996	0.990
Recall	0.955	0.944	0.987	0.935

4.2. Real data

In this experiment, the gauge section of injection molded cylindrical discontinuous glass fiber polypropylene tensile coupons were analyzed [13,14]. Projection images generated from 25 keV X-rays emissions from a monochromator incident on a rotating cylindrical specimen, were converted to a series of 16-bit, $1.3\mu m$ pixel size grayscale images using a gridded reconstruction algorithm for real-time tomography [15]. Typically, high intensity, moderate intensity and low intensity features detected on the greyscale images correspond to fibers, matrix and porosity, respectively. Despite the rich information in-situ tomography provides, images are occasionally fraught with random fluctuation of pixel values which are introduced during image acquisition and generation, despite conscientious efforts aimed at mitigating these effects. It is therefore imperative to develop robust segmentation algorithms capable of segmenting the fibers. Figure 9 shows fiber detection results in 6 consecutive 2D slices of a 3D microscopy image with dimension $301\times301\times301$. Different fibers are labeled with different color. As we can see, even though close contacted fibers exist in the dashed red circle in 2D slice, different fibers can be separated properly. Moreover, we can see the two detected purple fibers merge to one long fiber in the dashed red rectangle area, which implies the long fiber is curved in 3D space. Figure 10 presents the 3D visualization of fiber segmentation results by Fiji software.

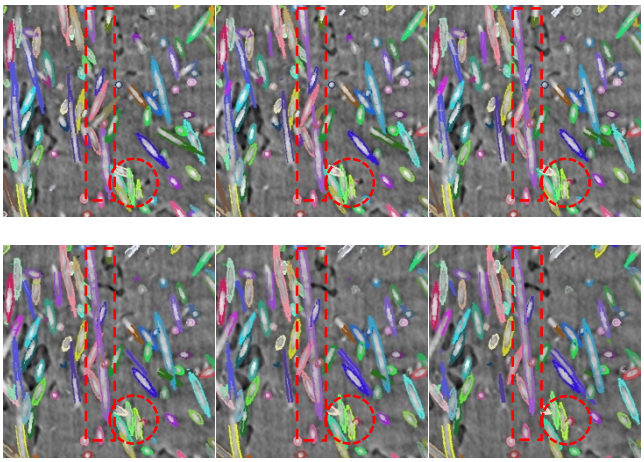

Figure 9. *6 consecutive 2D slices from 3D fiber detection results.*

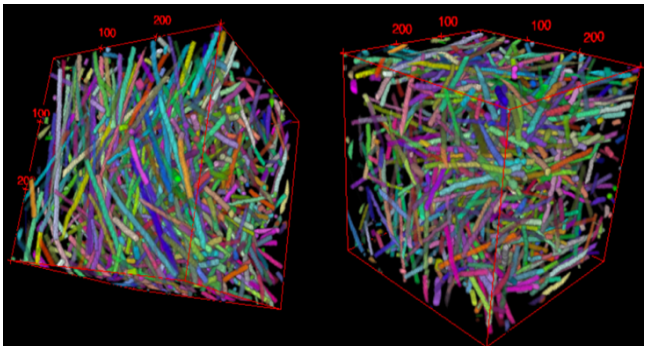

Figure 10. *3D visualization of the fiber segmentation.*

5. Conclusion

To model the fibers in fiber-reinforced composite materials images, we extend our previous 2D connected-tube MPP model to

a 3D connected-tube MPP model. The fibers are modeled as a series of short tubes connected by their joint areas. The experimental results on synthetic data and real data demonstrate the performance of our model.

Acknowledgement

The authors would like to acknowledge the support of the National Science Foundation through grant NSF CMMI MoM 16-62554.

References

[1] Fu, S.-Y, and Lauke B.L., "Effects of fiber length and fiber orientation distributions on the tensile strength of short-fiber-reinforced polymers," Composites Science and Technology, Vol. 56, pp. 1179-1190, 1996.

[2] M. Xia, H. Hamada, and Z. Maekawa, "Flexural Stiffness of Injection Molded Glass Fiber Reinforced Thermoplastics," International Polymer Processing, Vol. 10, No. 1, pp. 74- 81, 1995.

[3] S.-Y Fu, B.L. Lauke, E. Mäder, C.-H Yue., and X. Hu, "Tensile properties of short-glass-fiber- and short-carbon-fiber reinforced polypropylene composites," Composites Part A: Applied Science and Manufacturing, Vol. 31, pp. 1117- 1125, 2000.

[4] Fu, S.-Y., and Lauke B.L., "The elastic modulus of misaligned short-fiber-reinforced polymers," Composites Science and Technology, Vol. 58, pp. 389-400, 2000.

[5] R. Agyei and M. Sangid, "A supervised iterative approach to 3D microstructure reconstruction from acquired tomographic data of heterogeneous fibrous systems", Composite Structures, Vol. 206, pp. 234-246, 2018.

[6] P. A. Hessman, T. Riedel, F. Welschinger, K. Hornberger, T. Böhlke, "Microstructural analysis of short fiber reinforced thermoplastics based on x-ray micro-computed tomography", Composite Science Technology, Vol. 183, pp. 107752, 2019.

[7] O. Ronneberger, P. Fischer, and T. Brox, "U-net: Convolutional networks for biomedical image segmentation," in Medical Image Computing and Computer- Assisted Intervention (MICCAI), Cham, 2015, pp. 234–241, Springer.

[8] X. Descombes and J. Zerubia, "Marked point process in image analysis," IEEE Signal Processing Magazine, vol. 19, Issue 5, pp. 77–84, 2002.

[9] H. Zhao, M. L. Comer, and M. De Graef, "A unified markov random field/marked point process image model and its application to computational materials," in IEEE International Conference on Image Processing (ICIP). 2014, pp. 6101–6105, IEEE.

[10] X. Descombes, R. Minlos, and E. Zhizhina, "Object extraction using a stochastic birth-and- death dynamics in continuum," Journal of Mathematical Imaging and Vision, vol. 33, Issue 3, pp. 347–359, 2009.

[11] T. Li, M. Comer, and J. Zerubia, "A Connected-Tube MPP Model for Object Detection with Application to Materials and Remotely-Sensed Images," in IEEE International Conference on Image Processing (ICIP), Oct. 2018, pp. 1323–1327, IEEE.

[12] Xavier Descombes, "Multiple objects detection in biological images using a marked point process framework," Methods, vol. 115, pp. 2–8, 2017.

[13] I. Hanhan, R. Agyei, X. Xiao, and M. Sangid, "Comparing non-destructive 3D X-ray computed tomography with destructive optical microscopy for microstructural characterization of fiber reinforced composites", Composite Science Technology, Elsevier, Vol .184, pp. 107843, 2019.

[14] I. Hanhan, R.F. Agyei, X. Xiao and M.D. Sangid. "Predicting Microstructural Void Nucleation in Discontinuous Fiber Composites through coupled in-situ X-ray Tomography Experiments and Simulations." Nature Scientific Reports (2019). In press.

[15] D. Gurrsoy, F. De Carlo, X. Xiao, C. Jacobsen, "Tomopy: a framework for the analysis of synchrotron tomographic data", Journal of Synchrotron Radiation, Vol. 21, pp. 1188-1193, 2014.

JOIN US AT THE NEXT EI!

IS&T International Symposium on

Electronic Imaging

SCIENCE AND TECHNOLOGY

Imaging across applications . . . Where industry and academia meet!

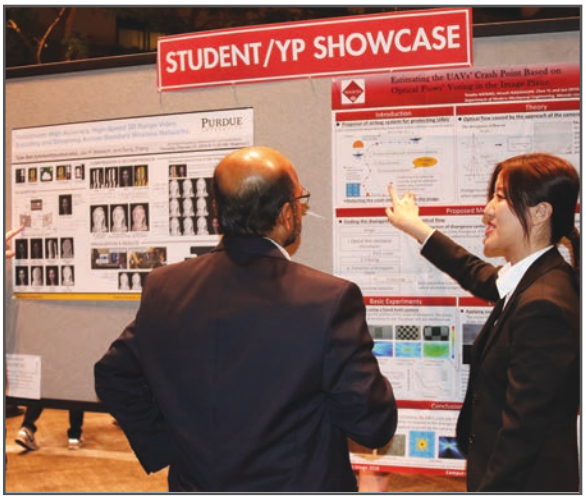

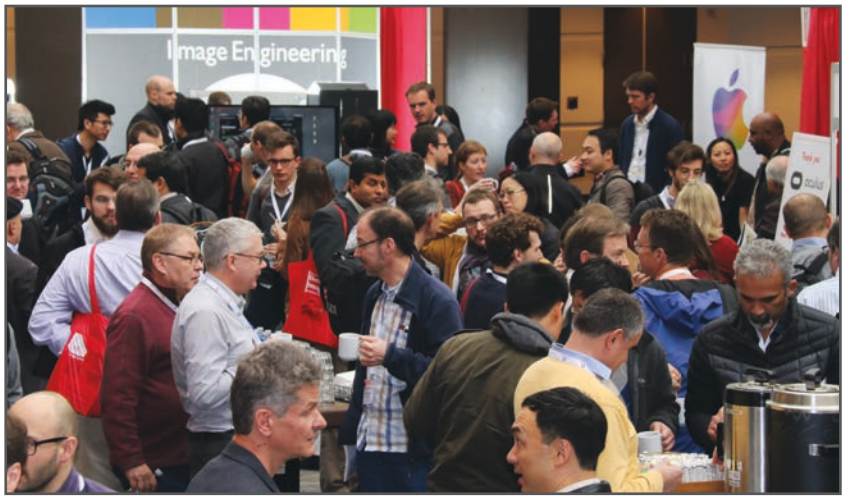

• SHORT COURSES • EXHIBITS • DEMONSTRATION SESSION • PLENARY TALKS •
• INTERACTIVE PAPER SESSION • SPECIAL EVENTS • TECHNICAL SESSIONS •

www.electronicimaging.org

IS&T
imaging.org